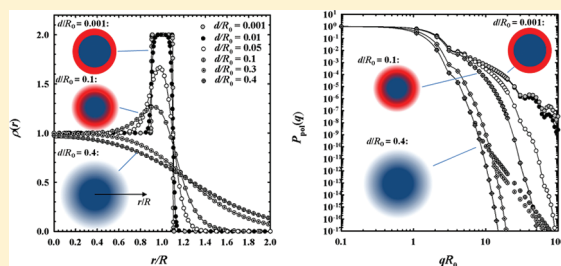


# Universal Analytical Scattering Form Factor for Shell–, Core–Shell, or Homogeneous Particles with Continuously Variable Density Profile Shape

Tobias Foster\*

University of Cologne, Institute for Physical Chemistry, Luxemburger Str. 16, 50939 Cologne, Germany

**ABSTRACT:** A novel analytical and continuous density distribution function with a widely variable shape is reported and used to derive an analytical scattering form factor that allows us to universally describe the scattering from particles with the radial density profile of homogeneous spheres, shells, or core–shell particles. Composed by the sum of two Fermi–Dirac distribution functions, the shape of the density profile can be altered continuously from step-like via Gaussian-like or parabolic to asymptotically hyperbolic by varying a single “shape parameter”,  $d$ . Using this density profile, the scattering form factor can be calculated numerically. An analytical form factor can be derived using an approximate expression for the original Fermi–Dirac distribution function. This approximation is accurate for sufficiently small rescaled shape parameters,  $d/R$  ( $R$  being the particle radius), up to values of  $d/R \approx 0.1$ , and thus captures step-like, Gaussian-like, and parabolic as well as asymptotically hyperbolic profile shapes. It is expected that this form factor is particularly useful in a model-dependent analysis of small-angle scattering data since the applied continuous and analytical function for the particle density profile can be compared directly with the density profile extracted from the data by model-free approaches like the generalized inverse Fourier transform method.



## INTRODUCTION

Small-angle scattering is a versatile and widely applied method for the microscopic structural characterization (length scale 1–100 nm) of a wide range of soft matter systems and colloidal dispersions.<sup>1,2</sup> Many of these systems consist of scattering particles that often exhibit an inhomogeneous internal structure of multiple domains being concentrically arranged around the particle center. Examples for such scattering particles are micro-emulsion droplets, micelles, vesicles, colloidal particles, or dendrimers. For the analysis of the respective scattering data, either model-dependent methods that assume a certain particle structure<sup>2,3</sup> can be applied, or model-independent methods can be used such as those based on the inverse Fourier-transform of the scattering data.<sup>4–8</sup> Model-dependent methods are particularly useful when the internal structure of the scattering particle is known from other experimental techniques (like microscopy methods), theoretical model predictions, or the composition of the sample. For instance, a known sample composition in combination with equations that add constraints over the volume and the scattering length allows us to suggest the internal structure of the scattering particle that can then be used as a starting point in such a model-dependent analysis. Thereby, the internal structure is described by a certain well-defined type of the radial density distribution function or density profile from which a (ideally analytical) scattering function is obtained. Such scattering functions can then be used to fit the experimental scattering data, allowing us (i) to extract relevant structural parameters such as the size and the size polydispersity of the

particles and (ii) to confirm their assumed internal structure. Model-independent methods do not assume a certain underlying particle density profile for the analysis of the scattering data but solve the inverse scattering problem by Fourier-transforming the scattering data (generalized indirect Fourier transform technique (GIFT), see refs 4–8 for more details). This procedure yields a pair distance distribution function that can be further deconvoluted to yield the radial density profile of the scattering particles. This density profile can then be applied to eventually validate the assumed density profile used in a model-dependent data analysis.

Analytical or numerical expressions for scattering functions used in model-dependent methods are available for a great variety of (i) different particle shapes like spheres,<sup>9</sup> disks,<sup>10</sup> ellipsoids,<sup>11</sup> cylinders,<sup>12</sup> wormlike chains,<sup>13–16</sup> and network junctions<sup>17</sup> as well as (ii) different radial density profiles that correspond to different internal structures of the particles, such as for instance homogeneous particles, shell-like particles, or core–shell particles.<sup>1–3</sup> In addition, respective scattering functions can be obtained for various functional forms of the radial density profile. The most basic functional form assumes a step-like behavior of the radial density profile, i.e., sharp boundaries of the concentric domains of different densities. Using this approach, Lord Rayleigh has derived the scattering function for a homogeneous sphere.<sup>6</sup> This approach can be used as the starting point for obtaining scattering

Received: May 4, 2011

Revised: July 1, 2011

Published: July 01, 2011

functions of shell-like or core–shell particles with sharp boundaries between the concentric domains of different density.<sup>1–3</sup> Such an approximation is particularly appropriate for modeling scattering data from colloids and solid particles,<sup>18–20</sup> and it has been used as well for describing scattering data from, for instance, micellar systems<sup>21–24</sup> and vesicles.<sup>25,26</sup> Consequently, these “basic” models have been applied to develop analytical scattering functions for more complex particle architectures, e.g., spherical particles with a particle core of homogeneous density, and polymer chains attached to the surface of the particle core.<sup>27–39</sup>

However, other types of scattering particles show radial density profiles that do not exhibit sharp boundaries between the domains of different density and are accordingly not appropriately described by the aforementioned step-like density profiles. Instead, such scattering particles are characterized by a smoother spatial variation of the radial density distribution. Examples are spherical polymer brushes with theoretically predicted power–law density profiles<sup>40–42</sup> from which semianalytical scattering functions have been derived<sup>43</sup> and successfully applied to interpret scattering data from block copolymer micelles.<sup>44</sup> Such power–law profiles can be approximated by a sequence of many concentric shells with sharp boundaries with only *small* changes of the density between neighboring shells.<sup>45</sup> Other examples are scattering functions for (i) free polymer chains with Gaussian density distribution<sup>46</sup> or exponential density profiles<sup>43</sup> or (ii) microgel particles<sup>28,47–49</sup> and block copolymer micelles<sup>28,50</sup> for which the radial density profile has been expressed by a piecewise function based on cubic b-splines.<sup>28,47–50</sup>

As another example, the scattering data from microemulsions with droplet microstructure turned out to require the form factor for a bare step-like density profile to be multiplied with an  $\exp[-q^2 S_R^2]$  term to improve the quality of the model fit of the data in the range of high absolute values of the scattering vector,  $q$ .<sup>51–54</sup> This term takes into account the “surface roughness”,<sup>51</sup>  $S_R$ , or “diffusivity”<sup>55</sup> of the amphiphilic film (surfactant monolayer that separates the droplet core from the continuous phase), i.e., the smooth change of the scattering length density profile across the amphiphilic film. This “diffuse” nature of the amphiphilic film arises from a penetration of solvent molecules into the amphiphilic film, the solvation of the surfactant molecules by the solvent molecules, positional fluctuations of the surfactant molecules within the amphiphilic film, and the frequent exchange of surfactant molecules between the amphiphilic film and the solvents.<sup>55</sup> To avoid the introduction of the additional  $\exp[-q^2 S_R^2]$  term and the surface roughness,  $S_R$ , as an additional structural parameter (in addition to the droplet radius, the thickness of the amphiphilic film, and the polydispersity of the droplet ensemble), an analytical form factor based on a Gaussian-like density profile for the amphiphilic film has been derived.<sup>55</sup> This model turned out to be appropriate to describe the scattering from droplet microemulsions with a shell-like density distribution, i.e., for droplets for which the scattering spectrum is dominated by the scattering arising solely from the amphiphilic film (so-called shell or film contrast conditions, i.e., equal scattering length or electron densities for the droplet core and the continuous phase that surrounds the droplets).<sup>55,56</sup> This Gaussian-like density profile for the amphiphilic film has also been confirmed by inverse Fourier-transform methods.<sup>57,58</sup>

Accordingly, for microemulsion droplets with a density distribution of a homogeneous sphere (so-called bulk contrast, i.e., equal scattering length or electron densities for the droplet core and the amphiphilic film), a step-like profile with a Gaussian-like

decay has been suggested<sup>56</sup> (a similar model has also been applied on scattering data from block copolymer micelles<sup>31,50</sup>), while for droplets with core–shell architecture a step-like profile for the droplet core and a Gaussian-like profile for the amphiphilic film has been applied.<sup>59,60</sup> However, this latter model fails under conditions where the core-scattering contribution modeled by the step-like function becomes significant (according to ref 61:  $(\rho_{\text{film}} - \rho_{\text{core}})/\rho_{\text{film}} \approx 0.02$ , i.e.,  $\rho_{\text{core}} \lesssim \rho_{\text{film}}$ ), as recently encountered in a SANS (small-angle neutron scattering) contrast variation study on CO<sub>2</sub>-in-water droplet microemulsions.<sup>61</sup> In this limit of a significant core-scattering contribution (relative to the scattering contribution of the amphiphilic film), it turned out that simply adding the step-like function and the Gaussian function yields a radial density profile that overestimates the film scattering. This leads to a high- $q$  behavior of the resulting scattering function that can only be compensated by unphysically large values of the thickness of the amphiphilic film.<sup>61</sup>

To overcome this limitation, an analytical expression for a closed and continuous radial density distribution is suggested here that (i) allows us to capture universally various functional forms of the density distribution such as step-like, Gaussian-like, parabolic, or asymptotically hyperbolic and (ii) is applicable for particles with different internal structures, such as homogeneous particles, shell-like particles, or core–shell particles. Being based on the sum of two Fermi–Dirac distribution functions, the functional forms can be varied continuously by changing a single “shape parameter”,  $d$ . This versatility of the Fermi–Dirac distribution function has been used in previous studies where a single Fermi–Dirac distribution function was applied to model the density distribution of polymer chains in the corona of block-copolymer micelles.<sup>33,37</sup> Furthermore, single Fermi–Dirac distribution functions have been applied as cutoff functions for the density profile of the polymer corona of block-copolymer micelles, ensuring that the density profile captures the finite polymer chain length.<sup>34–36</sup>

In the work presented here, it will be shown first how the sum of two Fermi–Dirac distribution functions can be utilized to calculate numerically the scattering form factors for polydisperse spherical scattering particles with a density distribution of homogeneous spheres, shells, or core–shell particles. In a next step, an approximate expression for the Fermi–Dirac distribution functions<sup>62</sup> (and references cited therein<sup>63–65</sup>) is used to derive analytical expressions for the scattering amplitudes and the scattering form factors for these scattering particles. Both models are then used to show how a systematic variation of the profile shape affects the behavior of the resulting scattering functions. This approach, being based on a simple, continuous analytical function for the density profile that is appropriate for a variety of different soft matter systems, is expected to be very useful for the model-dependent analysis of small-angle scattering data. Thereby, the closed and continuous (as opposed to piecewise) functional form of the applied density profiles allows them to be easily compared directly to the radial density profiles obtained from the pair distance distribution function that can be extracted by the aforementioned model-independent methods as the inverse Fourier-transform.<sup>4–8</sup> In addition, such an approach based on analytical equations for the density profile allows us to derive analytical expressions for relevant parameters of the scattering particles, such as the mean square radius that is given in eq 19 in ref 62.

## SCATTERING THEORY

The small-angle scattering arising from an individual scattering particle can be described by the normalized scattering form factor,  $P(q)$  (with  $P(q \rightarrow 0) = 1$ ), that for a spherically symmetric (isotropic), globular particle is related to the normalized scattering amplitude,  $A(q)$  (with  $A(q \rightarrow 0) = 1$ ) and its complex conjugate,  $A^*(q)$ , by<sup>1,2</sup>

$$P(q) = A(q) \cdot A^*(q) \quad (1)$$

For a spherically symmetric particle, the normalized amplitude  $A(q)$  is given by the Fourier transform of the radial density distribution function,  $\rho(r)$ , that describes the radial density profile of the scattering particle

$$\begin{aligned} A(q) &= \frac{1}{N_{\text{Part}}} \cdot \iiint \rho(r) \cdot \exp\{-i \cdot q \cdot r \cdot \cos \theta\} \cdot r^2 \cdot \sin \theta \cdot d\theta \cdot d\varphi \cdot dr \\ &= \frac{4\pi}{N_{\text{Part}}} \cdot \int_0^\infty \rho(r) \cdot r^2 \cdot \frac{\sin(q \cdot r)}{q \cdot r} \cdot dr \end{aligned} \quad (2)$$

Thereby, the normalization constant  $N_{\text{Part}}$  is given by

$$N_{\text{Part}} = \iiint \rho(r) \cdot r^2 \cdot \sin \theta \cdot d\theta \cdot d\varphi \cdot dr \quad (3)$$

A size polydispersity of the scattering particles will be included by applying an appropriate particle size distribution to the scattering form factor,  $P(q, R)$ , by solving the integral

$$P_{\text{Pol}}(q, R_0) = \frac{1}{N} \int_0^\infty V_{\text{Part}}^2 \cdot P(q, R) \cdot W(R, R_0, \sigma) \cdot dR \quad (4)$$

where  $V_{\text{Part}}$  is the volume of the scattering particle;  $W(R, R_0, \sigma)$  is the distribution function of the droplet radii  $R$  around their mean value  $R_0$ ; and  $N$  is the normalization constant (ensuring  $P_{\text{Pol}}(q \rightarrow 0, R_0) = 1$ )

$$N = \int_0^\infty V_{\text{Part}}^2 \cdot W(R, R_0, \sigma) \cdot dR \quad (5)$$

It is known that the introduction of size polydispersity effects is independent of the shape of the chosen size distribution for a sufficiently low width  $\sigma$  of the distribution.<sup>66</sup> Moreover, for the values of the polydispersity index,  $p = \sigma/R_0 \approx 0.2$ , that are often found in typical soft matter systems (e.g., droplet micro-emulsions<sup>55,56,67–69</sup>), it is not possible to precisely determine the shape of the size distribution function. In addition, the assumption of a Gaussian size distribution function often allows us to obtain an analytical solution of the integral in eq 4 (when the lower integration limit is set from 0 to  $-\infty$  which leads to a negligible error for a small polydispersity), as in the case of the approximate density profile,  $\rho_A(r)$ , used in this work (see below for more details). Thus, a Gaussian distribution function

$$W(R, R_0, \sigma) = \frac{1}{\sqrt{2\pi \cdot \sigma^2}} \cdot \exp\left\{-\frac{(R - R_0)^2}{2 \cdot \sigma^2}\right\} \quad (6)$$

will be used to account for the particle size polydispersity. It should be noted that the integrals involved in eq 4 can be solved analytically for the applied approximate density profile,  $\rho_A(r)$ , as well when a Schulz–Zimm distribution is used for  $W(R, R_0, \sigma)$ .<sup>38,39</sup>

First, a scattering form factor,  $P(q)$ , will be presented that is based on a density profile,  $\rho_{\text{FD}}(r)$ , given by the sum of two

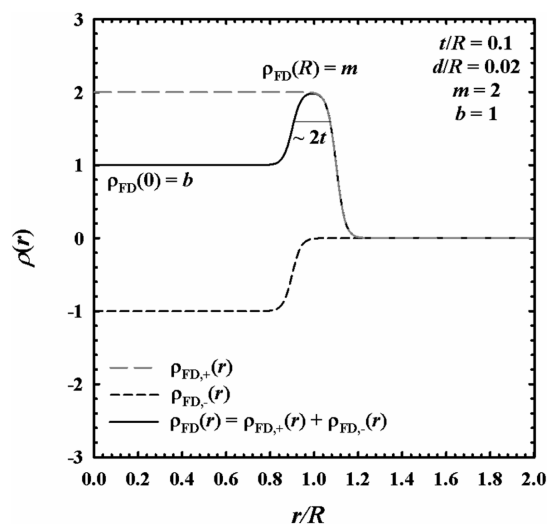


**Figure 1.** Radial density distribution function,  $\rho_{\text{FD}}(r)$ , based on the sum of two Fermi–Dirac distribution functions,  $\rho_{\text{FD},+}(r)$  and  $\rho_{\text{FD},-}(r)$ . For the chosen set of parameters,  $\rho_{\text{FD}}(r)$  corresponds to the density profile of a core–shell particle with constant core density,  $\rho_{\text{FD}}(0) = b = 1$ , and a density-maximum,  $\rho_{\text{FD}}(R) = m = 2$ , at the shell radius,  $R$ , whereby the thickness of the shell is given by  $2t$ . The shape of the profile can be altered by changing the shape parameter,  $d$ .

Fermi–Dirac distribution functions. For this density profile, the scattering amplitude and the form factor can be calculated numerically according to eqs 1 and 2. In a second step, an approximate expression,  $\rho_A(r)$ , for the original Fermi–Dirac distribution function<sup>62</sup> (and references cited therein<sup>63–65</sup>) will be used in eqs 1 and 2 to obtain an analytical expression for the scattering amplitude and the form factor.

**Numerical Model Using the Fermi–Dirac Distribution Function.** A universal expression for the density profile of scattering particles with an internal structure of homogeneous spheres, shell-like particles, or core–shell particles, and allowing us to continuously vary the profile shape, is obtained on the basis of a Fermi–Dirac distribution function<sup>70</sup>

$$\rho(r) = \frac{m}{1 + e^{(r-L)/d}} \quad (7)$$

For positive values of  $d$ , this function converges like  $\rho(r \rightarrow 0) \approx m$  (for  $L \gg d$ ) and  $\rho(r \rightarrow \infty) = 0$  while showing a decay around  $r \approx L$  that is sharp for small values of the “shape parameter”,  $d$  ( $d/L \ll 1$ ), and increasingly smooth as  $d/L$  increases ( $d/L \gtrsim 0.1$ ). This behavior is used to construct a density profile,  $\rho_{\text{FD}}(r)$ , by using a sum of two Fermi–Dirac distribution functions,  $\rho_{\text{FD},+}(r)$  and  $\rho_{\text{FD},-}(r)$ ,

$$\rho_{\text{FD}}(r) = \rho_{\text{FD},+}(r) + \rho_{\text{FD},-}(r) \quad (8)$$

whereby the two summands are given by

$$\rho_{\text{FD},+}(r) = \frac{m}{1 + e^{(r-R-t)/d}} \quad (9)$$

and

$$\rho_{\text{FD},-}(r) = \frac{b-m}{1 + e^{(r-R+t)/d}} \quad (10)$$

(the indices “+” and “−” refer to the fact that  $\rho_{\text{FD},+}(r) > 0$  and  $\rho_{\text{FD},-}(r) < 0$  for the case of  $m > 0$  and  $m > b$ ; see Figure 1).



Figure 1 shows the density profile,  $\rho_{\text{FD}}(r)$ , for a typical set of parameter values that are chosen as follows: to obtain a density profile,  $\rho_{\text{FD}}(r)$ , with a peak of defined width at  $r = R$ , the position  $r \approx L$  of the decay of the original Fermi–Dirac distribution function, eq 7, is shifted to  $L = R - t$  for  $\rho_{\text{FD},+}(r)$  and  $L = R + t$  for  $\rho_{\text{FD},-}(r)$ . Thus, the sum  $\rho_{\text{FD}}(r) = \rho_{\text{FD},+}(r) + \rho_{\text{FD},-}(r)$  has a peak at  $r = R$ , whereby the width of the peak is quantified by the parameter  $t$ . Thereby, the full width of the peak is equal to  $2t$  for values of the shape parameter,  $d$ , that are small compared to the radius ( $d/R \lesssim 0.01$ ), while the full width at half height becomes increasingly larger than  $2t$  the more  $d/R$  increases (for  $d/R \gtrsim 0.05$ ).

As indicated in Figure 1, the value of  $b = 1$  corresponds to the value of  $\rho_{\text{FD}}(r)$  at the origin, i.e.,  $\rho_{\text{FD}}(r \rightarrow 0) = b$ , while the parameter  $m = 2$  is a measure for the value of  $\rho_{\text{FD}}(r)$  at the maximum of the peak, i.e.,  $\rho_{\text{FD}}(r \rightarrow R) \approx m$  (note that for given values of  $b$  and  $m$  an increase in  $d/R$  in fact reduces the value of  $\rho_{\text{FD}}(r \rightarrow 0)$  and  $\rho_{\text{FD}}(r \rightarrow R)$ , as shown below). As in the original Fermi–Dirac distribution function in eq 7, the shape of the density profile,  $\rho_{\text{FD}}(r)$ , around  $r \approx R \pm t$  is controlled by the “shape parameter”,  $d$ . For small  $d/R \ll 1$ , a sharp decay is obtained that becomes increasingly smooth as  $d$  increases ( $d/R \gtrsim 0.01$ ), as will be shown in more detail below. For large  $r$ , the profile converges as  $\rho_{\text{FD}}(r \rightarrow \infty) = 0$ .

For the suggested density profile,  $\rho_{\text{FD}}(r)$ , it is not possible to obtain an analytical amplitude equation by solving eq 2. Accordingly, the polydisperse form factor according to eq 4 was evaluated numerically using Mathematica 7.0, whereby the integration was performed in the limits  $0 \leq R \leq 10R_0$  (the results shown here were calculated using a polydispersity index of  $p = \sigma/R_0 = 0.2$  which is a typical value for microemulsion droplets<sup>55,59,67,68</sup>).

**Analytical Form Factor Using an Approximate Expression for the Fermi–Dirac Distribution.** For the Fermi–Dirac distribution function, eq 7, an approximate expression has been presented<sup>62</sup> (and references cited therein<sup>63–65</sup>) that is exact in the limit  $d/R \ll 1$  and has been used to obtain an analytical solution for the scattering amplitude, eq 2. This result is applied here to obtain an analytical expression for the polydisperse form factor, eq 4. This is possible when (i) an appropriate particle size distribution function is used, such as for instance the Gaussian function, eq 6, and (ii) the lower integration limit is set from 0 to  $-\infty$  which leads to a negligible error for a small polydispersity.

As a starting point, an approximate density profile,  $\rho_{\text{A}}(r) \approx \rho_{\text{FD}}(r)$ , is obtained by using a sum of two approximate functions<sup>62</sup> for the Fermi–Dirac distribution functions,  $\rho_{\text{A},+}(r) \approx \rho_{\text{FD},+}(r)$  and  $\rho_{\text{A},-}(r) \approx \rho_{\text{FD},-}(r)$

$$\rho_{\text{A}}(r) = \rho_{\text{A},+}(r) + \rho_{\text{A},-}(r) \quad (11)$$

whereby the two summands are given by

$$\rho_{\text{A},+}(r) = \frac{m \cdot \sinh\left[\frac{R+t}{d}\right]}{\cosh\left[\frac{r}{d}\right] + \cosh\left[\frac{R+t}{d}\right]} \quad (12)$$

and

$$\rho_{\text{A},-}(r) = \frac{(b-m) \cdot \sinh\left[\frac{R-t}{d}\right]}{\cosh\left[\frac{r}{d}\right] + \cosh\left[\frac{R-t}{d}\right]} \quad (13)$$

Using eq 2, for both summands,  $\rho_{\text{A},+}(r)$  and  $\rho_{\text{A},-}(r)$ , of the approximate density profile,  $\rho_{\text{A}}(r)$ , analytical expressions for the normalized (i.e.,  $A(q \rightarrow 0) = 1$ ) scattering amplitudes can be calculated<sup>62</sup> (and the references cited therein<sup>63–65</sup>), namely

$$A_{\text{A},+}(q) = \frac{m}{N_{\text{Part},+}} \cdot 4d \cdot (\pi/q)^2 \cdot \text{Csch}[d\pi q] \cdot \{d\pi q \cdot \text{Coth}[d\pi q] \sin[q(R+t)] - q(R+t) \cos[q(R+t)]\} \quad (14)$$

and

$$A_{\text{A},-}(q) = \frac{b-m}{N_{\text{Part},-}} \cdot 4d \cdot (\pi/q)^2 \cdot \text{Csch}[d\pi q] \cdot \{d\pi q \cdot \text{Coth}[d\pi q] \sin[q(R-t)] - q(R-t) \cos[q(R-t)]\} \quad (15)$$

whereby “Csch” and “Coth” are the hyperbolic cosecant and the hyperbolic cotangent, respectively, and the normalization constants,  $N_{\text{Part},+}$  and  $N_{\text{Part},-}$ , are obtained with eq 3 as

$$N_{\text{Part},+} = m \cdot V_{\text{Part},+} = \frac{4}{3} \cdot m \cdot \pi \cdot (R+t) \cdot (d^2\pi^2 + (R+t)^2) \quad (16)$$

and

$$N_{\text{Part},-} = (b-m) \cdot V_{\text{Part},-} = \frac{4}{3} \cdot (b-m) \cdot \pi \cdot (R-t) \cdot (d^2\pi^2 + (R-t)^2) \quad (17)$$

These expressions are used to obtain the normalized scattering amplitude (i.e.,  $A_{\text{A}}(q \rightarrow 0) = 1$ ) that corresponds to the approximate density profile,  $\rho_{\text{A}}(r)$ , according to eq 2

$$A_{\text{A}}(q) = \frac{m \cdot V_{\text{Part},+} \cdot A_{\text{A},+}(q) + (b-m) \cdot V_{\text{Part},-} \cdot A_{\text{A},-}(q)}{m \cdot V_{\text{Part},+} + (b-m) \cdot V_{\text{Part},-}} \quad (18)$$

The respective normalized polydisperse form factor,  $P_{\text{Pol,A}}$ , is obtained by using eq 4 with the amplitude,  $A_{\text{A}}(q)$ , (eq 18) when (i) the Gaussian size distribution function 6 is used and (ii) the lower integration limit in eq 4 is set from 0 to  $-\infty$ . One obtains

$$P_{\text{Pol,A}}(q, R_0) = \frac{1}{N} \{p_1(q, R_0) + p_2(q, R_0) + p_3(q, R_0)\} \quad (19)$$

Thereby, the first term  $p_1(q, R_0)$  is given by

$$p_1(q, R_0) = m^2 \cdot \int_0^\infty V_{\text{Part},+}^2 \cdot A_{\text{A},+}^2(q) \cdot W(R, R_0, \sigma) \cdot dR \quad (20)$$

Note that  $p_1(q, R_0)$ , i.e., the result obtained when  $A_{\text{A},+}(q)$  and  $V_{\text{Part},+}$  alone are used in eqs 1 and 4, is the scattering form factor for the radial density profile of a homogeneous particle (i.e.,  $b = m$ ) with continuously variable decay of the density profile (see below). The other two summands in eq 19,  $p_2(q, R_0)$  and  $p_3(q, R_0)$ , are given by

$$p_2(q, R_0) = (b-m)^2 \cdot \int_0^\infty V_{\text{Part},-}^2 \cdot A_{\text{A},-}^2(q) \cdot W(R, R_0, \sigma) \cdot dR \quad (21)$$

and

$$p_3(q, R_0) = 2 \cdot m \cdot (b - m) \cdot \int_0^\infty V_{\text{Part},+} \cdot V_{\text{Part},-} \cdot A_{A,+}(q) \cdot A_{A,-}(q) \cdot W(R, R_0, \sigma) \cdot dR \quad (22)$$

The analytical results of eqs 20, 21, and 22 are given in the Appendix, as well as the normalization constant  $N$  that ensures  $P_{\text{Pol},A}(q \rightarrow 0, R_0) = 1$  and is obtained by using eq 5, whereby in the integrand the total volume of the scattering particle,  $V_{\text{Part}}$ , is replaced by  $m \cdot V_{\text{Part},+} + (b - m) \cdot V_{\text{Part},-}$ . For larger values of the rescaled shape parameter,  $d/R_0 \geq 0.1$ , the approximate profile,  $\rho_A(r)$ , was also used in a numerical evaluation of eq 4 to investigate the influence of deviations of  $\rho_A(r)$  from  $\rho_{\text{FD}}(r)$  for  $d/R_0 \geq 0.1$  on the obtained form factors. This numerical integration was done as well with Mathematica 7.0 with the integration limits  $0 \leq R \leq 10R_0$ , using the NIntegrate-command with the option of setting the maximum number of recursions (MaxRecursion) to 12.

## RESULTS AND DISCUSSION

Depending on the chosen values for the parameters  $b$  and  $m$ , and the rescaled parameters  $t/R_0$  and  $d/R_0$  used in the model described above ( $R_0$  is mean particle radius, see below), density profiles for particles with different types of internal structure are obtained, such as homogeneous particles, shell-like particles, or core-shell particles. In addition, the profile shape can be altered from a step-like to a more smooth variation of the density. In this section, it will be shown how the type, the shape, and the functional form of the density profile are governed by the chosen parameter values and how such variations of the particle density profile affect the particle scattering form factor. These calculations will be done for both the profile  $\rho_{\text{FD}}(r)$  based on the sum of two Fermi-Dirac distribution functions and the approximate profile,  $\rho_A(r)$ . Thereby it will (i) be shown how previously used approaches based on a single Fermi-Dirac distribution function<sup>33,37</sup> can be extended and (ii) be possible to estimate the quality of the approximate profile,  $\rho_A(r)$ , compared to the approach based on the sum of two Fermi-Dirac distribution functions. Throughout all figures shown here, the numerical results obtained using  $\rho_{\text{FD}}(r)$  will be shown as circular symbols, while the analytical results obtained using  $\rho_A(r)$  will be shown by the lines. The results obtained by the numerical integration using  $\rho_A(r)$  will be shown as diamond symbols. In all form factor calculations, a polydispersity of the radius of the scattering particles is included. This size polydispersity assumes a mean radius,  $R_0$ , of the ensemble of particles and is quantified by the standard deviation,  $\sigma$ , of the assumed Gaussian particle size distribution function (eq 6). Thereby, the standard deviation is set to  $\sigma/R_0 = 0.2$  which is a typical value for microemulsion droplets.<sup>55,59,67,68</sup>

**Shell Particles.** In the case of shell particles, the parameter  $b$  is set to  $b = 0$ , resulting in a radial density distribution function that exhibits a peak at  $r = R$ , as can be seen in Figure 2a. The width of the peak represents the thickness of the shell and is defined by the parameter  $t$ , whereby  $t/R_0 = 0.1$ . The height of the peak is given by the parameter  $m$ , whereby  $m = 2$ . For small values of the rescaled shape parameter,  $d/R_0 = 0.001$ , the radial density profile is step-like; i.e., there is a sharp transition from the region of zero density to the region of maximal density around  $r = R$ . As is clearly visible in Figure 2a, the transition between the regions of different density becomes smoother as the rescaled shape

parameter,  $d/R_0$ , is increased. For  $d/R_0 = 0.01$ , the transition is still sharp, but the edges are rounded instead of being sharp. As  $d/R_0$  is further increased to  $d/R_0 \geq 0.05$ , the density maximum around  $r = R$  becomes wider, while the density value at the maximum value of the density,  $\rho(R)$ , decreases although the value of the parameter  $m$  was set to  $m = 2$  in all calculations. The profile has a Gaussian shape for  $d/R_0 = 0.05$  (a Gaussian distribution function is shown by the cross-symbols and is calculated using a mean radius  $R$  and a standard deviation  $\sigma/R = 0.105$ ).

With the given resolution, the approximate profile,  $\rho_A(r)$ , shown as lines in Figure 2a, describes well the density values (circular symbols) calculated from the Fermi-Dirac-based profile,  $\rho_{\text{FD}}(r)$ , for sufficiently small values of the rescaled shape parameter,  $d/R_0 \leq 0.1$ . For the profile calculated with the larger value,  $d/R_0 = 0.3$ , however, the approximate profile,  $\rho_A(r)$  (line), clearly deviates from  $\rho_{\text{FD}}(r)$  (symbols) for small values of  $r/R$ , as indicated by the arrow in Figure 2a.

This  $d/R_0$ -dependent systematic variation of the profile shape affects the behavior of the respective scattering form factors shown in Figure 2b, plotted as a function of  $qR_0$ , i.e., the absolute value of the scattering vector,  $q$ , rescaled with the mean radius  $R_0$ . The form factors obtained for  $d/R_0 = 0.001$  and  $0.01$  almost fall on top of each other and show pronounced oscillations in the range of high  $q$ -values,  $qR_0 \geq 20$ . These oscillations are related to the thickness  $t/R_0 = 0.1$  of the shell and are thus observed despite the size polydispersity included in the calculation. In the same  $q$ -range,  $qR_0 \geq 20$ , the values of the form factor calculated for  $d/R_0 = 0.01$  are slightly smaller than the values for  $d/R_0 = 0.001$ . As the rescaled shape parameter,  $d/R_0$ , is further increased, the obtained form factors show stronger deviations from the form factors calculated with  $d/R_0 = 0.001$  and  $0.01$  in the range of high  $q$ -values, while only small deviations are observed for the given resolution in the range of small  $q$ -values. In particular, for  $d/R_0 \leq 0.1$ , the form factors are very similar in the range of small  $q$ -values,  $qR_0 \leq 2$ , for which the behavior of the form factor is dominated by the influence of the particle radius and the polydispersity. In the  $q$ -range of the first-order oscillation (i.e.,  $qR_0 \approx 2-3$ ), the deviations from the form factor calculated with  $d/R_0 = 0.001$  become stronger the more  $d/R_0$  is increased. Furthermore, for larger  $q$ -values,  $qR_0 > 2-3$ , the decay of the form factor (i) becomes the stronger and (ii) occurs at the lower values of  $qR_0$  the more  $d/R_0$  is increased. Thereby, the positions of the minima of the oscillations of the form factor in the range of high  $q$ -values,  $qR_0 \geq 20$ , are conserved when  $d/R_0$  is increased up to  $d/R_0 = 0.1$ , as these oscillations are related to the constant thickness  $t/R_0 = 0.1$  of the shell (note that the positions of these oscillations are shifted to lower values of  $qR_0$  when  $t/R_0$  is increased; thus, as will be demonstrated below, thicker shells with, e.g.,  $t/R_0 = 0.35$  might cause these oscillations to appear in a  $q$ -range of  $qR_0 \approx 5$  that is experimentally accessible by neutron or X-ray scattering for typical values of  $R_0 \approx 100$  Å).

Such a behavior has been reported before for spherical shells with a smooth and diffuse scattering length density profile,<sup>54,55,71-73</sup> as opposed to spherical shells with a sharp spatial variation of the density (as found for  $d/R_0 = 0.001$  in this work). While for shells with a sharp variation of the density a  $q^{-2}$ -behavior of the scattering pattern is obtained at high  $q$ -values,  $qR_0 > 4$ , a stronger decay of the form factor is observed when the underlying density profile is smoother, as observed here for the systematic increase of profile smoothness with increasing  $d/R_0$ .

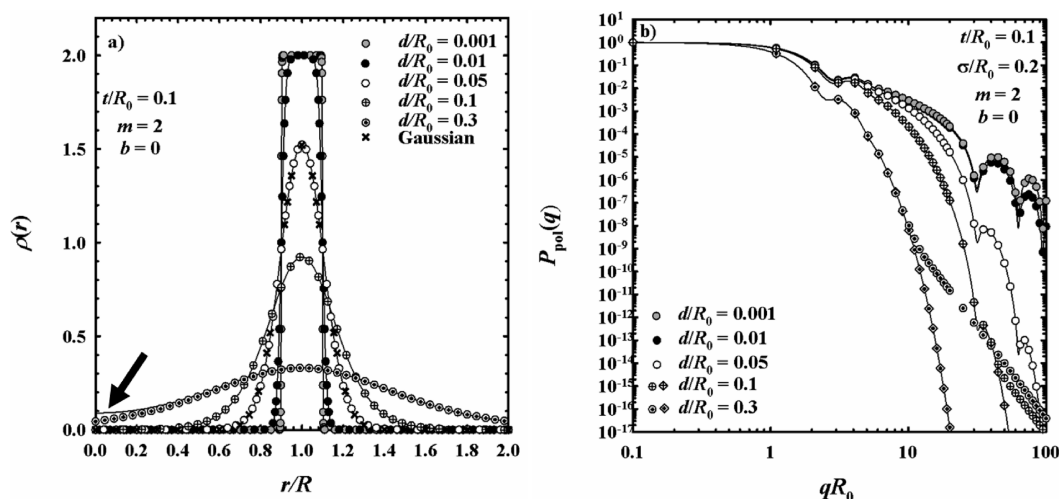


**Figure 2.** (a) Radial density distribution function,  $\rho(r)$ , for a shell particle (i.e.,  $\rho(0) = b = 0$ ) based on the Fermi–Dirac distribution function,  $\rho_{\text{FD}}(r)$  (symbols, except the crosses that show a Gaussian distribution function), and the approximation,  $\rho_A(r)$  (lines). With an increasing value of the rescaled shape parameter,  $d/R_0$ , the initially step-like decay (for  $d/R_0 = 0.001$ ) becomes increasingly smooth. For  $d/R_0 = 0.3$ ,  $\rho_A(r)$  deviates from  $\rho_{\text{FD}}(r)$  for small  $r/R$ , as indicated by the arrow. (b) Numerical (circles and diamonds) and analytical (lines) calculation of the form factor,  $P_{\text{pol}}(q)$ , for polydisperse shell particles having a mean radius  $R_0$  and the radial density profiles shown in (a), as a function of the rescaled scattering vector,  $qR_0$ . As  $\rho_A(r)$  differs from  $\rho_{\text{FD}}(r)$  for  $d/R_0 \geq 0.1$ , the numerical results using  $\rho_{\text{FD}}(r)$  (circles) deviate from the analytical results at high  $qR_0$ . Contrarily, the numerical results using  $\rho_A(r)$  (diamonds) perfectly reproduce the analytical results.

(Note that the  $q^{-2}$ -behavior for shells with a sharp variation of the density and the decay of the form factor in general is not affected by an increase of the thickness  $t/R_0$  of the shell. Instead, the decay of the form factor solely depends on the parameter  $d/R_0$ , i.e., the profile shape. An increase of  $t/R_0$  just shifts the position of the oscillations in the range of high  $q$ -values to lower  $qR_0$ , as mentioned above, without changing the decaying envelope of the form factor.)

This trend continues when the rescaled shape parameter is further increased to  $d/R_0 = 0.3$ , causing the first-order oscillation of the form factor to set in at a  $qR_0 \approx 0.5$ . Accordingly, in the  $q$ -range of this first-order oscillation, the values of the form factor are significantly smaller for  $d/R_0 = 0.3$  than the respective form factor values obtained for  $d/R_0 \leq 0.1$ . In addition, with an increasing rescaled shape parameter,  $d/R_0 \geq 0.1$ , the form factor (circular symbols in Figure 2b) obtained numerically from the original Fermi–Dirac profile,  $\rho_{\text{FD}}(r)$ , begins to show deviations from the respective analytically calculated form factor (lines) at high  $q$ -values. A comparison of the form factors calculated with  $d/R_0 = 0.1$  and  $d/R_0 = 0.3$  shows that these deviations appear at lower  $q$ -values for the larger value of  $d/R_0 = 0.3$ . To find the reason for the deviation of the form factor calculated numerically using  $\rho_{\text{FD}}(r)$  from the analytical result using the approximate profile,  $\rho_A(r)$ , this latter approximate profile,  $\rho_A(r)$ , was used in the numerical calculation procedure of the form factor. Thereby, it turned out that this numerically calculated form factor using  $\rho_A(r)$  (diamond symbols in Figure 2b) perfectly recovers the analytical form factor based on  $\rho_A(r)$ . Thus, it can be concluded that the deviations of the numerical form factor based on the original Fermi–Dirac profile,  $\rho_{\text{FD}}(r)$ , from an analytical form factor based on the approximate profile,  $\rho_A(r)$ , arise from small deviations of  $\rho_A(r)$  from  $\rho_{\text{FD}}(r)$ , which are well visible in Figure 2a for  $d/R_0 = 0.3$  (indicated by the arrow).

**Core–Shell Particles.** The density profile of a core–shell particle is obtained when the parameter  $b$  obeys the condition

$0 < b \neq m$ , whereby  $m$  specifies the height of the density maximum that represents the particle shell. Thus, choosing  $b = 1$  and  $m = 2$  leads to a radial density distribution function that exhibits a constant core density (defined by  $b = 1$ ) and a peak at  $r = R$  for sufficiently small  $d/R_0 \leq 0.1$ , as can be seen in Figure 3a. As before, the shape of the profile around the density maximum can be continuously varied from step-like to smooth by increasing the rescaled shape parameter,  $d/R_0$ . When  $d/R_0$  is increased above  $d/R_0 > 0.1$ , the maximum in the density profile disappears, and the constant core density continuously decreases with increasing  $r/R$ . In addition, for the given resolution, deviations of the approximate profile,  $\rho_A(r)$  (lines), from the original Fermi–Dirac profile,  $\rho_{\text{FD}}(r)$  (symbols), are visible for  $d/R_0 \geq 0.4$  at small values of  $r/R$ , as indicated by the arrow in the inset in Figure 3a.

The  $d/R_0$ -dependent variations of the density profile lead to systematic changes of the resulting form factors. In particular, for small values of  $d/R_0 \leq 0.01$ , the form factors are almost identical, except the small deviation in the range of high  $q$ -values,  $qR_0 \geq 20$ , where pronounced form factor oscillations are observed that are related to the thickness  $t/R_0 = 0.1$  of the shell. With increasing  $d/R_0$ , the form factors decay more strongly, and the decay sets in at smaller values of  $qR_0$  the larger  $d/R_0$  becomes. Accordingly, with increasing  $d/R_0$ , increasing deviations of the form factors from the ones calculated with  $d/R_0 \leq 0.01$  appear. Compared to the case of spherical shells described above, for larger  $d/R_0 \geq 0.05$  less pronounced oscillations are observed in the range of high  $q$ -values. However, as before the deviations of the approximate profile,  $\rho_A(r)$ , from the original Fermi–Dirac profile,  $\rho_{\text{FD}}(r)$ , cause deviations of the form factor obtained numerically using  $\rho_{\text{FD}}(r)$  (circular symbols) from the analytical form factor using  $\rho_A(r)$  (lines) in the range of high  $q$ -values. When the form factor is calculated numerically using the approximate profile,  $\rho_A(r)$  (diamond symbols), the analytical form factor is recovered.

**Homogeneous Particles.** When the parameters  $b$  and  $m$  are chosen so that  $0 < b = m = 2$ , the density profile of a



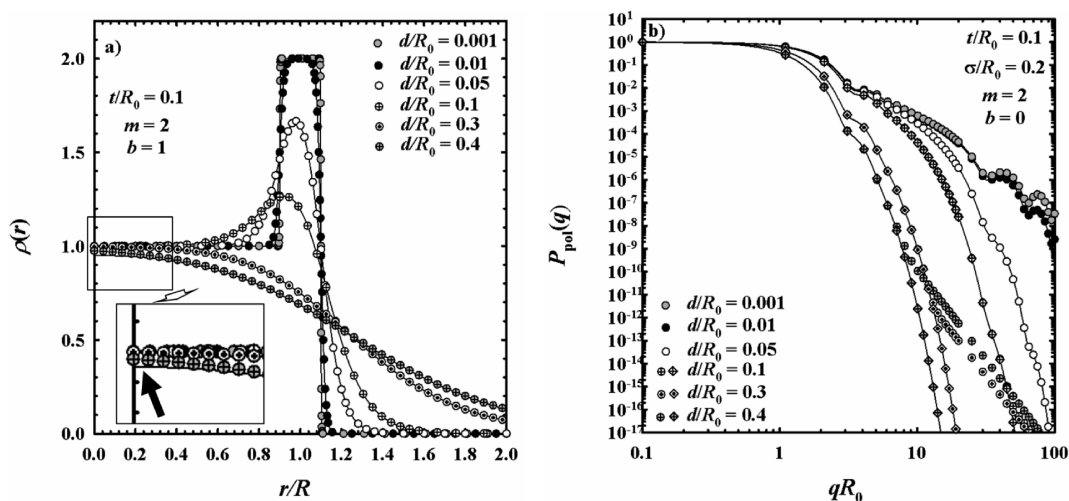


**Figure 3.** (a) Radial density distribution function,  $\rho(r)$ , for a core-shell particle (i.e.,  $\rho(0) = b = 1 < m$ ) based on the Fermi-Dirac distribution function,  $\rho_{\text{FD}}(r)$  (symbols), and the approximation,  $\rho_{\text{A}}(r)$  (lines). With an increasing value of the rescaled shape parameter,  $d/R_0$ , the initially step-like decay (for  $d/R_0 = 0.001$ ) becomes increasingly smooth, and the peak becomes less pronounced. For  $d/R_0 = 0.4$ ,  $\rho_{\text{A}}(r)$  deviates from  $\rho_{\text{FD}}(r)$  for small  $r/R$ , as indicated by the arrow in the inset figure. (b) Numerical (circles and diamonds) and analytical (lines) calculation of the form factor,  $P_{\text{pol}}(q)$ , for polydisperse core-shell particles having a mean radius  $R_0$  and the radial density profiles shown in (a), as a function of the rescaled scattering vector,  $qR_0$ . As  $\rho_{\text{A}}(r)$  differs from  $\rho_{\text{FD}}(r)$  for  $d/R_0 \geq 0.1$ , the numerical results using  $\rho_{\text{FD}}(r)$  (circles) deviate from the analytical results at high  $qR_0$ . Contrarily, the numerical results using  $\rho_{\text{A}}(r)$  (diamonds) perfectly reproduce the analytical results.

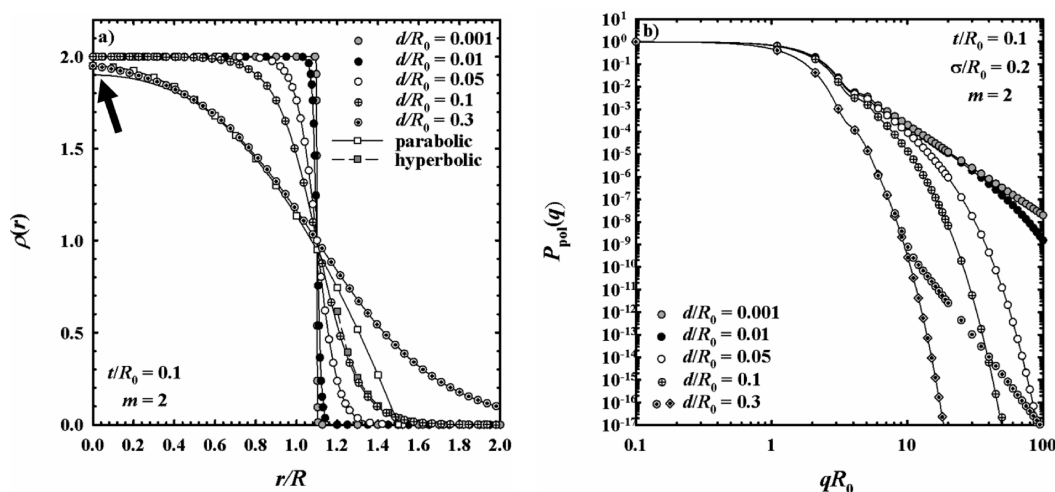


**Figure 4.** (a) Radial density distribution function,  $\rho(r)$ , for a particle with a homogeneous core (i.e.,  $\rho(0) = b = m$ ) based on the Fermi-Dirac distribution function,  $\rho_{\text{FD}}(r)$  (symbols), and the approximation,  $\rho_{\text{A}}(r)$  (lines). For  $d/R_0 = 0.3$ ,  $\rho_{\text{A}}(r)$  deviates from  $\rho_{\text{FD}}(r)$  for small  $r/R$ , as indicated by the arrow. While, for  $d/R_0 = 0.3$ ,  $\rho(r)$  has a parabolic shape for  $r \lesssim R$  (empty squares), the distribution function shows an asymptotically ( $r \gtrsim R$ ) hyperbolic behavior for  $d/R_0 = 0.1$  (filled squares). (b) Numerical (circles and diamonds) and analytical (lines) calculation of the form factor,  $P_{\text{pol}}(q)$ , for polydisperse particles ( $\sigma/R_0 = 0.2$ ) with homogeneous core having a mean radius  $R_0$  (and a thickness  $t$  of the interfacial region) and the radial density profiles shown in (a), as a function of the rescaled scattering vector,  $qR_0$ . As  $\rho_{\text{A}}(r)$  differs from  $\rho_{\text{FD}}(r)$  for  $d/R_0 \geq 0.3$ , the numerical results using  $\rho_{\text{FD}}(r)$  (circles) deviate from the analytical results at high  $qR_0$ . Contrarily, the numerical results using  $\rho_{\text{A}}(r)$  (diamonds) perfectly reproduce the analytical results.

homogeneous particle is obtained, exhibiting a constant core density that decays to its limiting value,  $\rho(r \rightarrow \infty) = 0$ , with increasing  $r/R$  without going through a density maximum (Figure 4a); the radius of the particle is given by  $R + t$ , whereby  $t$  corresponds to the thickness of the interfacial layer in this case. Since the term  $b - m$  in  $\rho_{\text{FD},-}(r)$  (eq 10) and  $\rho_{\text{A},-}(r)$  (eq 13) vanishes in this case of equal parameters  $b = m$ , the density profile for such homogeneous particles is given solely by  $\rho_{\text{FD},+}(r)$  (eq 9) and  $\rho_{\text{A},+}(r)$  (eq 12), respectively.

As shown in Figure 4a, this decay of the profile with increasing  $r/R$  is observed for various values of the rescaled shape

parameter,  $d/R_0$ , whereby the decay can be changed continuously from step-like to smooth by increasing  $d/R_0$ . While for  $d/R_0 = 0.001$  a step-like behavior with a sharp transition of the density is observed, for  $d/R_0 = 0.01$  the transition is still sharp; however, the edges are rounded instead of being sharp. This trend continues when  $d/R_0$  is further increased, leading to a profile for  $d/R_0 = 0.3$  that is parabolic for  $r \lesssim R$ , as indicated by the open square symbols in Figure 4a. The shown parabolic function has the form  $\rho(r) = a - (r/r_0)^n$ , whereby the parameters are chosen as  $a = b = 2$ ,  $r_0 = R + t$ , and  $n = 2.15 \approx 2$ . This parabolic function is mathematically equivalent to the parabolic density

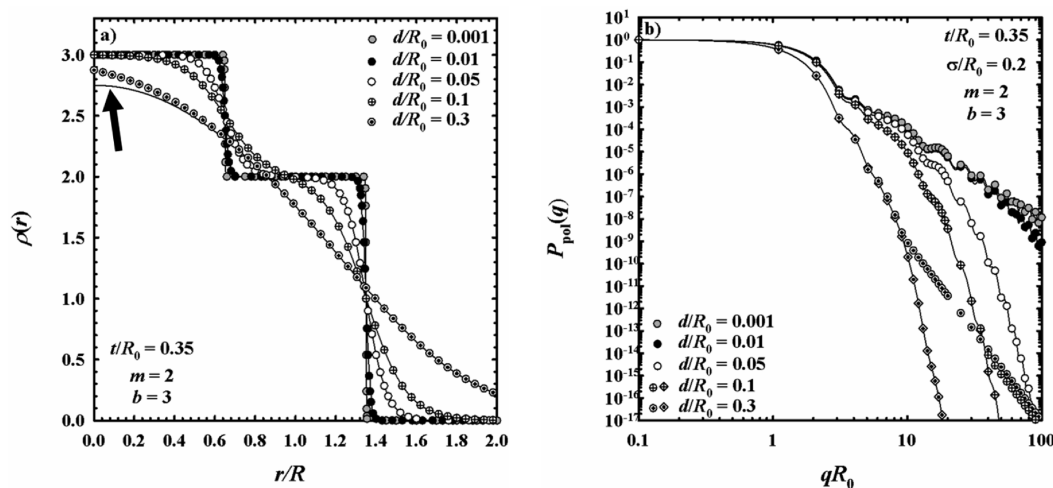


**Figure 5.** (a) Radial density distribution function,  $\rho(r)$ , for a multilayer particle with a stepwise decrease of the density (i.e.,  $\rho(0) = b > m$ ) which is based on the Fermi–Dirac distribution function,  $\rho_{FD}(r)$  (symbols), or the approximation,  $\rho_A(r)$  (lines). For  $d/R_0 = 0.3$ ,  $\rho_A(r)$  deviates from  $\rho_{FD}(r)$  for small  $r/R$ , as indicated by the arrow. The rescaled thickness of the low density layer is  $t/R_0 = 0.35$ . (b) Numerical (circles and diamonds) and analytical (lines) calculation of the form factor,  $P_{pol}(q)$ , for the polydisperse ( $\sigma/R_0 = 0.2$ ) multilayer particles having a mean radius  $R_0$  and the radial density profiles shown in (a), as a function of the rescaled scattering vector,  $qR_0$ . As  $\rho_A(r)$  differs from  $\rho_{FD}(r)$  for  $d/R_0 \geq 0.1$ , the numerical results using  $\rho_{FD}(r)$  (circles) deviate from the analytical results at high  $qR_0$ . Contrarily, the numerical results using  $\rho_A(r)$  (diamonds) perfectly reproduce the analytical results.

profiles that are theoretically predicted (with  $n = 2$ ) for planar polymer brushes.<sup>74,75</sup> The asymptotic behavior (i.e., for  $r > R$ ) of the suggested profiles,  $\rho_{FD}(r)$  and  $\rho_A(r)$ , is hyperbolic, as shown in Figure 4a by the filled square symbols for the profile calculated with  $d/R_0 = 0.1$ . The hyperbolic function that is used to model the profiles  $\rho_{FD}(r)$  and  $\rho_A(r)$  in the range  $r > R$  has the form  $\rho(r) = (r - r_0)^{-n} + c$ , whereby the parameters are chosen as  $r_0 = 0.25R$ ,  $n = 3$ , and  $c = -0.08 \approx 0$ . As indicated by the arrow in Figure 4a, for  $d/R_0 = 0.3$  the approximate profile,  $\rho_A(r)$  (line), deviates from the Fermi–Dirac-based profile,  $\rho_{FD}(r)$  (circular symbols), at small values of  $r/R$ .

The numerical and analytical form factors, calculated for the density profiles of a homogeneous particle defined by the criterion  $0 < b = m = 2$ , are shown in Figure 4b. Thereby, the respective analytical scattering amplitude is given solely by  $A_{A,+}(q)$  (eq 14) since  $A_{A,-}(q)$  (eq 15) vanishes because of  $b = m$ . Thus, the analytical form factor for polydisperse homogeneous spheres is given solely by  $p_1(q, R_0)$  (eq 20). For the step-like profile obtained for  $d/R_0 = 0.001$ , the resulting form factor shows a  $q^{-4}$ -behavior at high  $q$ -values  $qR_0 \gtrsim 5$  that is typical for the scattering from homogeneous spheres.<sup>9</sup> As observed in the other cases described above, with an increasing value of  $d/R_0$  and the underlying density profile becoming smoother, the form factors decay more strongly with increasing  $qR_0$ . Accordingly, their deviations from the form factor calculated with  $d/R_0 = 0.001$  set in at the smaller values of  $qR_0$  the larger  $d/R_0$  becomes, and thus these deviations become already more pronounced in the  $q$ -range of the first oscillation,  $qR_0 \approx 3$ . Despite being calculated with the same rescaled standard deviation,  $\sigma/R_0 = 0.2$ , of the particle size distribution function (eq 6) than the form factors in the previous cases, no oscillations are observed in the scattering patterns shown in Figure 4b at high  $q$ -values,  $qR_0 \gtrsim 5$ . This is explained by the underlying density profiles of the homogeneous particles that do not contain a smaller length scale (compared to  $R_0$ ) that causes significant scattering. Contrarily, the previous cases contain the thickness  $t/R_0 = 0.1$  of the shell with a density value  $m$  that is significantly different from the core

density  $b$ , thus causing oscillations in the scattering pattern at  $qR_0 \gtrsim 5$ . In addition, deviations of the numerically obtained form factor using the Fermi–Dirac-based profile,  $\rho_{FD}(r)$  (circular symbols), from the analytical form factor (lines) are visible only for  $d/R_0 \geq 0.3$ , instead of appearing already for  $d/R_0 = 0.1$  as in the previous cases. As the numerical form factor using the approximate density profile,  $\rho_A(r)$  (diamond symbols), recovers the analytical result, it can be concluded that the deviations of the numerical form factor using  $\rho_{FD}(r)$  arise from the deviations of  $\rho_A(r)$  from  $\rho_{FD}(r)$ , as indicated by the arrow in Figure 4a.

**Multilayer Particles.** The condition  $0 < b \neq m$  can also be fulfilled by choosing  $b > m$ , instead of using  $b < m$  as above in Figure 3. As a representative case, the radial density profiles using  $b = 3$  and  $m = 2$  are shown in Figure 5a for various values of  $d/R_0$ , leading to a radial density profile with a constant core density and lower density in the interfacial layer around  $r = R$ . Thereby, a thickness of the interfacial layer of  $t/R_0 = 0.35$  is applied here for a better visualization of the multiple layer structure of this profile (note that a smaller value of  $t/R_0 = 0.1$  was used in all previous cases). While for  $d/R_0 = 0.001$  a step-like behavior with sharp transitions between the regions of different density is observed, an increasing value of  $d/R_0$  causes the edges of the profile steps to become rounded and the density variations to become smoother. When the rescaled shape parameter is increased to  $d/R_0 = 0.3$ , the multilayer structure disappears, and the core density decays continuously with increasing  $r/R$  without passing through a density step in the interfacial region around  $r = R$ . In addition, for  $d/R_0 = 0.3$  the approximate profile,  $\rho_A(r)$  (line), deviates from the Fermi–Dirac-based profile,  $\rho_{FD}(r)$  (circular symbols), as indicated by the arrow in Figure 5a.

The resulting form factors are shown in Figure 5b. They follow the trend observed in the previous cases and show a stronger decay with increasing  $qR_0$  when the rescaled shape parameter,  $d/R_0$ , is increased. Thus, an increase in  $d/R_0$  causes increasingly stronger deviations of the resulting form factors from the form factor calculated for  $d/R_0 = 0.001$ , also in the  $q$ -range of the first oscillation. For all applied values of  $d/R_0$ , the form factors show



pronounced oscillations in the range of high  $q$ -values  $qR_0 \gtrsim 5$ , arising from the thickness of the interfacial layer of  $t/R_0 = 0.35$ . Since this value for  $t/R_0$  is larger than the thickness  $t/R_0 = 0.1$  of the shells used in the cases shown above, the related oscillations are observed here at smaller  $qR_0 \gtrsim 5$ , compared to  $qR_0 \gtrsim 20$  for which the respective oscillations are found with  $t/R_0 = 0.1$ . For  $d/R_0 \geq 0.1$ , the numerically obtained form factors using the Fermi–Dirac-based profile,  $\rho_{\text{FD}}(r)$  (circular symbols), deviate from the respective analytical form factors (lines) based on the approximate profile  $\rho_{\text{A}}(r)$ . As before, a numerical calculation of the form factor using  $\rho_{\text{A}}(r)$  recovers the analytical result, so that it can be concluded that the deviations obtained when  $\rho_{\text{FD}}(r)$  is used arise from the deviation of  $\rho_{\text{A}}(r)$  from  $\rho_{\text{FD}}(r)$  (see Figure Sa).

## CONCLUSION

A novel scattering form factor has been suggested that is based on a continuous analytical radial density distribution function that captures universally the density profiles of homogeneous spheres, shell-like particles, or core–shell particles while allowing us to vary continuously the shape of the respective profile. The radial density distribution function is calculated as the sum of two Fermi–Dirac distribution functions and has a shape that can be altered continuously from step-like via Gaussian-like or parabolic to asymptotically hyperbolic by varying the rescaled shape parameter,  $d/R_0$ . From this Fermi–Dirac-based model, a scattering form factor can be calculated numerically. An analytical form factor can be derived using an approximate expression for the original Fermi–Dirac distribution functions that is accurate for sufficiently small values of  $d/R_0 \lesssim 0.1$ .

For all the different internal architectures of the scattering particles investigated here, the systematic  $d/R_0$ -dependent variation of the profile shape characteristically affects the behavior of the corresponding scattering form factors. In particular, the decay of the scattering form factors with increasing rescaled scattering vector,  $qR_0$ , becomes steeper and more pronounced the more smooth the underlying density profile becomes, i.e., the larger  $d/R_0$  is. Contrarily, in the cases of a significant density of the interfacial layer of the scattering particles, an increase of the thickness  $t/R_0$  of this layer does not affect the steepness of the decay of the form factor but shifts the oscillations that are related to this length scale  $t/R_0$  to smaller values of  $qR_0$ . Thus, this study shows that the contrary influences of (i) the profile shape (related to  $d/R_0$ ) and (ii) the different length scales (related to  $t/R_0$ ) that define the particle architecture are expected to be well distinguished in the resulting scattering patterns.

Both presented approaches, being based on analytical functions for density profiles that are appropriate for a variety of different soft matter systems, are expected to be very useful for a model-dependent analysis of small-angle scattering data. The applied closed and continuous (as opposed to piecewise) functional form of the density profiles can then be compared directly to the radial density profiles extracted by the mentioned model-independent inverse Fourier-transform methods.<sup>4–8</sup> This was recently demonstrated in a SANS (small-angle neutron scattering) contrast variation study on CO<sub>2</sub>-in-water droplet microemulsions,<sup>61</sup> where the fits of the scattering data using the model presented here were perfectly confirmed by the density profiles deconvoluted from the pair distance distribution functions obtained in the model-independent generalized inverse Fourier transform method (GIFT) applied to the same data.<sup>61</sup>

## APPENDIX

The first term,  $p_1(q, R_0)$ , of the form factor 19 is given by the integral 20 that can be analytically solved (when the lower integration limit is set from 0 to  $-\infty$ ) as

$$p_1(q, R_0) = a_1 \cdot \{p_{11}(q, R_0) + p_{12}(q, R_0) + p_{13}(q, R_0) + p_{14}(q, R_0)\} \quad (23)$$

with the prefactor

$$a_1 = \frac{1}{q^2} 4d^2 m^2 \pi^4 \text{Csch}[d\pi q]^2 \quad (24)$$

and the expressions

$$p_{11}(q, R_0) = \{d^2 \pi^2 - R_0^2 - \sigma^2 - 2R_0 t - t^2\} \cdot \text{Csch}[d\pi q]^2 \quad (25)$$

$$p_{12}(q, R_0) = \{d^2 \pi^2 + R_0^2 + \sigma^2 + 2R_0 t + t^2\} \cdot \text{Cosh}[2d\pi q] \cdot \text{Csch}[d\pi q]^2 \quad (26)$$

$$p_{13}(q, R_0) = (-2)e^{-2q^2 \sigma^2} \{4q^2 \sigma^4 - R_0^2 - \sigma^2 - 2R_0 t - t^2\} \text{Cos}[2q(R_0 + t)] + d^2 \pi^2 \text{Cos}[2q(R_0 + t)] \cdot \text{Coth}[d\pi q]^2 \quad (27)$$

and

$$p_{14}(q, R_0) = (-2)e^{-2q^2 \sigma^2} \{4q\sigma^2(R_0 + t)\text{Sin}[2q(R_0 + t)] + 4d\pi \text{Coth}[d\pi q]q\sigma^2 \text{Cos}[2q(R_0 + t)] + 2d\pi \text{Coth}[d\pi q](R_0 + t)\text{Sin}[2q(R_0 + t)]\} \quad (28)$$

The second term,  $p_2(q, R_0)$ , of the form factor 19 is given by the integral 21 that can be analytically solved (when the lower integration limit is set from 0 to  $-\infty$ ) as

$$p_2(q, R_0) = a_2 \cdot \{p_{21}(q, R_0) + p_{22}(q, R_0) + p_{23}(q, R_0) + p_{24}(q, R_0)\} \quad (29)$$

with the prefactor

$$a_2 = \frac{1}{q^2} 4d^2 (b - m)^2 \pi^4 \text{Csch}[d\pi q]^2 \quad (30)$$

and the expressions

$$p_{21}(q, R_0) = \{d^2 \pi^2 - R_0^2 - \sigma^2 + 2R_0 t - t^2\} \cdot \text{Csch}[d\pi q]^2 \quad (31)$$

$$p_{22}(q, R_0) = \{d^2 \pi^2 + R_0^2 + \sigma^2 - 2R_0 t + t^2\} \cdot \text{Cosh}[2d\pi q] \cdot \text{Csch}[d\pi q]^2 \quad (32)$$

$$p_{23}(q, R_0) = (-2)e^{-2q^2 \sigma^2} \{4q^2 \sigma^4 - R_0^2 - \sigma^2 + 2R_0 t - t^2\} \text{Cos}[2q(R_0 - t)] + d^2 \pi^2 \text{Cos}[2q(R_0 - t)] \cdot \text{Coth}[d\pi q]^2 \quad (33)$$

and

$$p_{24}(q, R_0) = (-2)e^{-2q^2\sigma^2} \{4q\sigma^2(R_0 - t)\sin[2q(R_0 - t)] \\ + 4d\pi \coth[d\pi q]q\sigma^2 \cos[2q(R_0 - t)] \\ + 2d\pi \coth[d\pi q](R_0 - t)\sin[2q(R_0 - t)]\} \quad (34)$$

The third term,  $p_3(q, R_0)$ , of the form factor 19 is given by the integral 22 that can be analytically solved (when the lower integration limit is set from 0 to  $-\infty$ ) as

$$p_3(q, R_0) = a_3 \cdot \{p_{31}(q, R_0) + p_{32}(q, R_0) \\ + p_{33}(q, R_0) + p_{34}(q, R_0)\} \quad (35)$$

with the prefactor

$$a_3 = \frac{1}{q^2} 16d^2(b - m)m\pi^4 \operatorname{Csch}[d\pi q]^2 \quad (36)$$

and the expressions

$$p_{31}(q, R_0) = \{R_0^2 + \sigma^2 - t^2\} \cdot \cos[2qt] \quad (37)$$

$$p_{32}(q, R_0) = d^2\pi^2 \cos[2qt] \coth[d\pi q]^2 \\ + 2d\pi t \coth[d\pi q] \sin[2qt] \quad (38)$$

$$p_{33}(q, R_0) = (-2)e^{-2q^2\sigma^2} \{(4q^2\sigma^4 - R_0^2 - \sigma^2 + t^2)\cos[2qR_0] \\ + d^2\pi^2 \cos[2qR_0] \coth[d\pi q]^2\} \quad (39)$$

and

$$p_{34}(q, R_0) = (-2)e^{-2q^2\sigma^2} \{4qR_0\sigma^2 \sin[2qR_0] \\ + 2d\pi \coth[d\pi q](2q\sigma^2 \cos[2qR_0] \\ + R_0 \sin[2qR_0])\} \quad (40)$$

The normalization constant  $N$ , ensuring  $P_{\text{Pol,A}}(q \rightarrow 0, R_0) = 1$ , is obtained using eq 5 as

$$N = n_1^2 + (n_2^2 + 2n_1n_3)\sigma^2 + 3(n_3^2 + 2n_2n_4)\sigma^4 \\ + 15n_4^2\sigma^4 \quad (41)$$

with the expressions

$$n_1 = \frac{4}{3}d^2b\pi^3R_0 + \frac{4}{3}b\pi R_0^3 - \frac{4}{3}d^2(b - m)\pi^3t \\ + \frac{4}{3}d^2m\pi^3t - 4(b - m)\pi R_0^2t + 4m\pi R_0^2t \\ + 4b\pi R_0t^2 - \frac{4}{3}(b - m)\pi t^3 + \frac{4}{3}m\pi t^3 \quad (42)$$

$$n_2 = \frac{4}{3}d^2b\pi^3 + 4b\pi R_0^2 - 8(b - m)\pi R_0t \\ + 8m\pi R_0t + 4b\pi t^2 \quad (43)$$

$$n_3 = 4b\pi R_0 - 4(b - m)\pi t + 4m\pi t \quad (44)$$

and

$$n_4 = \frac{4}{3}b\pi \quad (45)$$

## AUTHOR INFORMATION

### Corresponding Author

\*Phone: +49-221-470-7336. Fax: +49-221-470-5104. E-mail: tobias.foster@uni-koeln.de.

## ACKNOWLEDGMENT

I wish to thank Thomas Sottmann, Michael Klostermann, and Reinhard Strey for fruitful discussions in the context of this work and Thomas Sottmann for his careful revision of the manuscript. I am indebted to Prof. Reinhard Strey for his continuous support of my work. Funding by the Alexander von Humboldt-foundation (Bonn, Germany, Feodor Lynen postdoctoral fellowship) is gratefully acknowledged.

## REFERENCES

- (1) Higgins, J. S.; Benoit, H. C. *Polymers and Neutron Scattering*; Clarendon Press: Oxford, 1994; Vol. 8.
- (2) *Neutrons, x-Rays and Light: Scattering Methods applied to Soft Condensed Matter*; Lindner, P.; Zemb, T., Eds.; Elsevier Science B.V.: Amsterdam, 2002.
- (3) Pedersen, J. S. *Adv. Colloid Interface Sci.* **1997**, *70*, 171.
- (4) Glatter, O. J. *Appl. Crystallogr.* **1977**, *10*, 415.
- (5) BrunnerPopela, J.; Glatter, O. J. *Appl. Crystallogr.* **1997**, *30*, 431.
- (6) Mittelbach, R.; Glatter, O. J. *Appl. Crystallogr.* **1998**, *31*, 600.
- (7) Weyerich, B.; Brunner-Popela, J.; Glatter, O. J. *Appl. Crystallogr.* **1999**, *32*, 197.
- (8) Fritz, G.; Glatter, O. J. *Phys.: Condens. Matter* **2006**, *18*, S2403.
- (9) Rayleigh, L. *Proc. R. Soc. London* **1911**, A84, 24.
- (10) Kratky, O.; Porod, G. *J. Colloid Sci.* **1949**, *4*, 35.
- (11) Guinier, A. *Ann. Phys.* **1939**, *12*, 161.
- (12) Fournet, G. *Bull. Soc. Fr. Mineral. Crist.* **1951**, *74*, 39.
- (13) Pedersen, J. S.; Schurtenberger, P. *Macromolecules* **1996**, *29*, 7602.
- (14) Pedersen, J. S.; Schurtenberger, P. *J. Appl. Crystallogr.* **1996**, *29*, 646.
- (15) Jerke, G.; Pedersen, J. S.; Egelhaaf, S. U.; Schurtenberger, P. *Phys. Rev. E* **1997**, *56*, 5772.
- (16) Pedersen, J. S.; Laso, M.; Schurtenberger, P. *Phys. Rev. E* **1996**, *54*, R5917.
- (17) Foster, T.; Safran, S. A.; Sottmann, T.; Strey, R. *J. Chem. Phys.* **2007**, *127*, 204711.
- (18) Markovic, I.; Ottewill, R. H. *Colloid Polym. Sci.* **1986**, *264*, 65.
- (19) Ottewill, R. H.; Sinagra, E.; Macdonald, I. P.; Marsh, J. F.; Heenan, R. K. *Colloid Polym. Sci.* **1992**, *270*, 602.
- (20) Moonen, J.; Dekruif, C. G.; Vrij, A.; Bantle, S. *Colloid Polym. Sci.* **1988**, *266*, 836.
- (21) Tabony, J. *Mol. Phys.* **1984**, *51*, 975.
- (22) Hayter, J. B.; Penfold, J. *J. Chem. Soc., Faraday Trans. I* **1981**, *77*, 1851.
- (23) Triolo, R.; Hayter, J. B.; Magid, L. J.; Johnson, J. S. *J. Chem. Phys.* **1983**, *79*, 1977.
- (24) Zemb, T. N.; Barnes, I. S.; Derian, P.-J.; Ninham, B. W. *Prog. Colloid Polym. Sci.* **1990**, *81*, 20.
- (25) Pedersen, J. S. *Eur. Biophys. J. Biophys. Lett.* **1993**, *22*, 79.
- (26) Bauer, R.; Behan, M.; Clarke, D.; Hansen, S.; Jones, G.; Mortensen, K.; Pedersen, J. S. *Eur. Biophys. J. Biophys. Lett.* **1992**, *21*, 129.
- (27) Pedersen, J. S.; Gerstenberg, M. C. *Macromolecules* **1996**, *29*, 1363.
- (28) Pedersen, J. S.; Gerstenberg, M. C. *Colloids Surf., A-Physicochem. Eng. Aspects* **2003**, *213*, 175.
- (29) Pedersen, J. S. *J. Chem. Phys.* **2001**, *114*, 2839.
- (30) Pedersen, J. S.; Hamley, I. W.; Ryu, C. Y.; Lodge, T. P. *Macromolecules* **2000**, *33*, 542.
- (31) Pedersen, J. S.; Svaneborg, C.; Almdal, K.; Hamley, I. W.; Young, R. N. *Macromolecules* **2003**, *36*, 416.

- (32) Arleth, L.; Svensson, B.; Mortensen, K.; Pedersen, J. S.; Olsson, U. *Langmuir* **2007**, *23*, 2117.
- (33) Won, Y. Y.; Davis, H. T.; Bates, F. S.; Agamalian, M.; Wignall, G. D. *J. Phys. Chem. B* **2000**, *104*, 7134.
- (34) Poppe, A.; Willner, L.; Allgaier, J.; Stellbrink, J.; Richter, D. *Macromolecules* **1997**, *30*, 7462.
- (35) Willner, L.; Poppe, A.; Allgaier, J.; Monkenbusch, M.; Lindner, P.; Richter, D. *Europhys. Lett.* **2000**, *51*, 628.
- (36) Lund, R.; Willner, L.; Stellbrink, J.; Radulescu, A.; Richter, D. *Macromolecules* **2004**, *37*, 9984.
- (37) Lund, R.; Willner, L.; Lindner, P.; Richtert, D. *Macromolecules* **2009**, *42*, 2686.
- (38) Plestil, J. *J. Appl. Crystallogr.* **2000**, *33*, 600.
- (39) Plestil, J.; Kriz, J.; Tuzar, Z.; Prochazka, K.; Melnichenko, Y. B.; Wignall, G. D.; Talingting, M. R.; Munk, P.; Webber, S. E. *Macromol. Chem. Phys.* **2001**, *202*, 553.
- (40) Alexander, S. *J. Phys.* **1977**, *38*, 983.
- (41) Degennes, P. G. *J. Phys.* **1976**, *37*, 1445.
- (42) Daoud, M.; Cotton, J. P. *J. Phys.* **1982**, *43*, 531.
- (43) Förster, S.; Burger, C. *Macromolecules* **1998**, *31*, 879.
- (44) Förster, S.; Wenz, E.; Lindner, P. *Phys. Rev. Lett.* **1996**, *77*, 95.
- (45) Nayeri, M.; Zackrisson, M.; Bergenholtz, J. *J. Phys. Chem. B* **2009**, *113*, 8296.
- (46) Debye, P. *J. Phys. Colloid Chem.* **1947**, *51*, 18.
- (47) Berndt, I.; Pedersen, J. S.; Lindner, P.; Richtering, W. *Langmuir* **2006**, *22*, 459.
- (48) Berndt, I.; Pedersen, J. S.; Richtering, W. *J. Am. Chem. Soc.* **2005**, *127*, 9372.
- (49) Berndt, I.; Pedersen, J. S.; Richtering, W. *Angew. Chem., Int. Ed.* **2006**, *45*, 1737.
- (50) Svaneborg, C.; Pedersen, J. S. *Macromolecules* **2002**, *35*, 1028.
- (51) Arleth, L.; Pedersen, J. S. *Phys. Rev. E* **2001**, *63*, 061406-1.
- (52) Endo, H.; Mihailescu, M.; Monkenbusch, M.; Allgaier, J.; Gompper, G.; Richter, D.; Jakobs, B.; Sottmann, T.; Strey, R.; Grillo, I. *J. Chem. Phys.* **2001**, *115*, 580.
- (53) Sottmann, T.; Strey, R.; Chen, S. H. *J. Chem. Phys.* **1997**, *106*, 6483.
- (54) Strey, R.; Winkler, J.; Magid, L. *J. Phys. Chem.* **1991**, *95*, 7502.
- (55) Gradzielski, M.; Langevin, D.; Magid, L.; Strey, R. *J. Phys. Chem.* **1995**, *99*, 13232.
- (56) Bagger-Jorgensen, H.; Olsson, U.; Mortensen, K. *Langmuir* **1997**, *13*, 1413.
- (57) Strey, R.; Glatter, O.; Schubert, K. V.; Kaler, E. W. *J. Chem. Phys.* **1996**, *105*, 1175.
- (58) Brunner-Popela, J.; Mittelbach, R.; Strey, R.; Schubert, K. V.; Kaler, E. W.; Glatter, O. *J. Chem. Phys.* **1999**, *110*, 10623.
- (59) Foster, T.; Sottmann, T.; Schweins, R.; Strey, R. *J. Chem. Phys.* **2008**, *128*, 054502.
- (60) Foster, T.; Sottmann, T.; Schweins, R.; Strey, R. *J. Chem. Phys.* **2008**, *128*, 064902.
- (61) Klostermann, M.; Foster, T.; Strey, R.; Sottmann, T.; Schweins, R.; Lindner, P.; Glatter, O. *PCCP* **2011** (submitted).
- (62) Sprung, D. W. L.; Martorell, J. *J. Phys. A: Math. Gen.* **1997**, *30*, 6525.
- (63) Eldyshev, Y. N.; Lukanyov, V. N.; Pol, Y. S. *Yad. Fiz.* **1972**, *16*, 506.
- (64) Burov, V. V.; Ivanyuk, F. A.; Konstantinov, B. D. *Yad. Fiz.* **1975**, *22*, 1142.
- (65) Buck, B.; Pilt, A. A. *Nuclear Phys. A* **1977**, *280*, 133.
- (66) Kotlarchyk, M.; Chen, S. H.; Huang, J. S.; Kim, M. W. *Phys. Rev. A* **1984**, *29*, 2054.
- (67) Gradzielski, M.; Langevin, D.; Sottmann, T.; Strey, R. *J. Chem. Phys.* **1997**, *106*, 8232.
- (68) Hellweg, T.; Langevin, D. *Phys. Rev. E* **1998**, *57*, 6825.
- (69) Hellweg, T.; Brulet, A.; Sottmann, T. *Phys. Chem. Chem. Phys.* **2000**, *2*, 5168.
- (70) Kittel, C. *Introduction to solid state physics*, 8th ed.; Wiley: New York, 2005.
- (71) Schubert, K. V.; Strey, R. *J. Chem. Phys.* **1991**, *95*, 8532.
- (72) Ruland, W. *J. Appl. Crystallogr.* **1971**, *4*, 70.
- (73) Lee, D. D.; Chen, S. H. *Phys. Rev. Lett.* **1994**, *73*, 106.
- (74) Milner, S. T.; Witten, T. A.; Cates, M. E. *Europhys. Lett.* **1988**, *5*, 413.
- (75) Zhulina, E. B.; Borisov, O. V.; Priamitsyn, V. A. *J. Colloid Interface Sci.* **1990**, *137*, 495.